In vivo molecular imaging of peripheral amyloidosis using heparin-binding peptides

Jonathan S. Wall[a,b,1], Tina Richey[a], Alan Stuckey[b], Robert Donnell[c], Sallie Macy[a], Emily B. Martin[a], Angela Williams[a], Keiichi Higuchi[d], and Stephen J. Kennel[a,b]

Departments of [a]Medicine and [b]Radiology, University of Tennessee Graduate School of Medicine, Knoxville, TN 37920; [c]Department of Pathobiology, University of Tennessee College of Veterinary Medicine, Knoxville, TN 37996; and [d]Department of Aging Biology, Institute on Aging and Adaptation, Shinshu University Graduate School of Medicine, Matsumoto 390-8621, Japan

Edited by Leslie Lars Iversen, University of Oxford, Oxford, United Kingdom, and approved July 12, 2011 (received for review March 3, 2011)

Heparan sulfate proteoglycans (HSPGs) are ubiquitous components of pathologic amyloid deposits in the organs of patients with disorders such as Alzheimer's disease or systemic light chain (AL) or reactive (AA) amyloidosis. Molecular imaging methods for early detection are limited and generally unavailable outside the United Kingdom. Therefore, there is an urgent need to develop novel, specific amyloidophilic radiotracers for imaging to assist in diagnosis, prognostication, and monitoring response to therapy. Amyloid-associated HSPG can be differentiated from HSPG found in surrounding healthy cells and tissues by the preferential binding of certain HS-reactive single chain variable fragments and therefore, represents a biomarker that can be targeted specifically with appropriate reagents. Using a murine model of AA amyloidosis, we have examined the in vivo amyloid reactivity of seven heparin-binding peptides by using single photon emission and X-ray computed tomographic imaging, microautoradiography, and tissue biodistribution measurements. All of the peptides bound amyloid deposits within 1 h post-injection, but the extent of the reactivity differed widely, which was evidenced by image quality and grain density in autoradiographs. One radiolabeled peptide bound specifically to murine AA amyloid in the liver, spleen, kidney, adrenal, heart, and pancreas with such avidity that it was observed in single photon emission tomography images as late as 24 h post-injection. In addition, a biotinylated form of this peptide was shown histochemically to bind human AA, ALκ, ALλ, transthyretin amyloidosis (ATTR), and Aβ amyloid deposits in tissue sections. These basic heparin-binding peptides recognize murine and human amyloid deposits in both in vivo and ex vivo tissues and therefore, have potential as radiotracers for the noninvasive molecular imaging of amyloid deposits in situ.

Amyloid is a complex, pathologic extracellular deposit composed principally of protein fibrils associated with heparan sulfate proteoglycans (HSPG) and accessory molecules such as serum amyloid P component (SAP). The fibrils are formed from partially misfolded proteins or fragments that deposit in organs and tissues and cause architectural damage that leads to dysfunction and ultimately, death (1). Amyloidosis is invariably associated with diseases such as Alzheimer's disease (AD), light chain (AL) amyloidosis, and reactive (AA) amyloidosis. In addition, amyloid may be a complicating pathology in type II diabetes, cases of chronic inflammation such as rheumatoid arthritis, and the plasma cell dyscrasia multiple myeloma (2, 3). In each case, the amyloid fibril is composed of a disease-specific protein or peptide (e.g., the Aβ peptide in patients with AD, light chains in patients with AL amyloidosis and multiple myeloma, or islet amyloid polypeptide precursor protein in patients with type II diabetes). Although varying in etiology and site of deposition, the amyloid deposits share remarkable structural homogeneity consisting of unbranched fibrils of ~10 nm in diameter and comprising proteins that adopt a cross-β pleated sheet secondary structure, which was evidenced by X-ray diffraction and NMR (4, 5). Furthermore, all amyloids contain significant concentrations of HSPG (6–8), and each amyloid binds the pentraxin protein SAP in a calcium-dependent manner (9). Finally, all amyloids can be detected histochemically by virtue of their interaction with the dyes thioflavin T and Congo red (10, 11).

The presence of HSPG in all amyloid deposits, regardless of the type of protein fibril, has been well-established, and its importance in the etiology of the disease has been shown in vivo and in vitro (12–14). Organs that overexpressed the heparanase enzyme in a transgenic mouse model and therefore, lacked significant sulfated proteoglycans did not support AA amyloidogenesis (13). Furthermore, soluble HS mimetics, such as polyvinyl sulfonate, have been used successfully to inhibit AA amyloidosis in mice; however, derivative molecules evaluated in human clinical trials have not yielded similarly dramatic results (15, 16). Amyloid-associated HSPG has been shown by chromatographic analyses (17–20) and reaction with antibodies (21, 22) to be biochemically distinct from that found in the extracellular matrices and plasma membranes of healthy tissues. Notably, amyloid-associated HSPGs seem to be more heavily sulfated than those HSPGs in normal tissue. The high concentration and unique chemical structure renders it a potential biomarker that may be targeted with suitable imaging reagents for the purpose of diagnosis, prognostication, and monitoring response to therapy.

Presently, in the United States, there are no approved imaging techniques to document the whole-body burden or organ distribution of visceral amyloid in patients. Whole-body planar scintigraphy or single photon emission tomography (SPECT) using iodine-123 (^{123}I) -labeled SAP has been used in Europe for more than two decades (9, 23). It provides images of amyloid load that can be used to compliment routine diagnosis by histochemical analysis of tissue biopsies, aid in prognostication, and document response to therapy (24, 25). Although ^{123}I-SAP scintigraphy is the most common imaging technique for the detection of amyloid in the peripheral organs, other methods using ^{99m}Tc-aprotinin and ^{99m}Tc-3,3-diphosphon-1,2-propanodicarboxylic acid for imaging cardiac amyloid and ATTR, respectively, are also available (26–30). These methods are rarely used, however, because of the nonspecific nature of the interaction. The use of SAP for amyloid imaging in the United States has not been approved by the Food and Drug Administration because of the human plasma source of this protein; therefore, alternative strategies are required to address the need for amyloid imaging in the United States.

Author contributions: J.S.W. and S.J.K. designed research; J.S.W., R.D., T.R., and S.J.K. analyzed data; K.H. contributed new reagents/analytic tools; T.R., A.S., S.M., A.W., and S.J.K. performed research; and J.S.W., E.B.M., and S.J.K. wrote the paper.

Conflict of interest statement: J.S.W. and S.J.K. are inventors on a patent describing this technology.

This article is a PNAS Direct Submission.

[1]To whom correspondence should be addressed. E-mail: jwall@utmck.edu.

See Author Summary on page 13899.

This article contains supporting information online at www.pnas.org/lookup/suppl/doi:10.1073/pnas.1103247108/-/DCSupplemental.

Based on our finding that certain single chain variable fragments (scFv) were reactive with a heparin-like, hypersulfated form of HSPG that was unique to amyloid in our murine model of AA (22), we evaluated a series of seven heparin-binding peptides as potential imaging agents for amyloid in vivo by using small animal SPECT imaging, tissue biodistribution measurements, and microautoradiography. The best of these peptides bound rapidly and specifically with amyloid in vivo and in sufficient concentrations to be imaged by SPECT at 24 h postinjection (pi). The retention of this peptide in amyloid-laden organs in vivo was shown to increase linearly with the amyloid load, which was evidenced by a comparison with qualitative Congo red scoring of stained tissue sections. In addition, we have observed no reactivity of this peptide within healthy organs. Finally, this peptide reacted specifically with human AA, AL, ATTR, and Aβ amyloid in formalin-fixed paraffin-embedded tissue sections. These properties support the evaluation of this basic peptide as an imaging agent for the clinical detection of peripheral organ amyloidosis in man by using molecular imaging.

Results

The precise mass of each purified peptide was confirmed by MS based on the amino acid sequence (Table 1). Only fractions containing peptides of the correct mass were used in imaging studies. The heparin-binding characteristics of each purified peptide were assessed using high salt elution from a heparin column. Each of the peptides bound to the heparin column, with peptides p2, p3, p4, and p5 eluting as a symmetrical peak as the salt concentration increased (Fig. 1*A*). In contrast, the p1, p6, and p7 peptides exhibited broader and asymmetric elution profiles. In general, the affinity of each of the peptides for the column-bound heparin correlated linearly with their total and net charge (Fig. 1 *B* and *C*, respectively). When considering the net charge, heparin reactivity of the peptides decreased: p1 > p6 > p4 > p5 = p3 > p7 > p2.

Each peptide was radioiodinated, and the amyloid-binding efficacy was determined at 1 and 4 h pi in mice with severe systemic AA amyloidosis or age-matched healthy WT animals. The biodistribution of radioactivity in weighed samples of excised tissues was assessed. At 1 h pi, peptides p1, p3, p4, and p5 were selectively retained in the liver [11.6%, 6.0%, 5.8%, and 12.5% injected dose (ID)/g, respectively], spleen (11.5%, 3.0%, 5.6%, and 15.9% ID/g, respectively), and pancreas (7.1%, 5.6%, 6.3%, and 10.0% ID/g, respectively), sites of high concentrations of AA amyloid in these mice as confirmed by Congo red staining of each tissue sample. Relative to retention in WT mice, each of these peptides was present at two- to sevenfold greater amounts in the organs of mice with AA (Tables 2 and 3). Notably, peptide p5 was present in the highest amounts and exhibited AA to WT uptake ratios for liver and spleen of ∼5 and 8, respectively. Based on the retention in the liver at 1 h, as a measure of amyloid-binding efficacy, the peptides were graded p5 > p1 > p6 > p4 ∼ p3 > p7 > p2.

At 4 h pi, all of the peptides, with the exception of p4 and p7, showed greater than twofold difference in hepatic and splenic retention in mice with AA compared with WT animals (Tables S1 and S2). Each of the peptides seemed to be cleared at a similar rate from the blood pool of AA mice, which was evidenced by the similar percent ID per gram radioactivity in the muscle and lung (sites of little or no AA amyloid). At 4 h pi, peptide p5 exhibited the highest AA to WT ratio of ∼10 for the liver and >20 for the spleen. This specific uptake was confirmed by calculating the tissue to muscle ratios for AA and WT mice at 1 h pi (Fig. S1).

SPECT/computed tomography (CT) imaging of each peptide in WT and AA mice at 1 and 4 h pi was used to determine the lead candidate for clinical diagnostic imaging. In the AA mice, peptides p1, p5, and to a lesser degree, p6 accumulated in the abdominal organs (liver, spleen, pancreas, and kidneys) in sufficiently high concentrations to be visible by SPECT imaging at 1 h pi (Fig. 2). In contrast, radioactivity was only observed in the kidneys, stomach, and thyroid of AA mice that received ^{125}I-p2, and only the thyroid and stomach (sites of $^{125}I^-$ accumulation) were evidenced in mice administered ^{125}I-p3, -p4, or -p7. Images of amyloid-free WT mice at 1 h pi showed radioactivity only within the stomach and thyroid, regardless of the injected peptide (Fig. 2). At 4 h pi, ^{125}I-p1 and -p5 remained detectable in the liver and spleen (and possibly pancreas) of AA mice (Fig. 2). In AA mice that received the other peptides, only the stomach and thyroid were seen in the SPECT images, which is indicative of weak peptide binding to amyloid; catabolism and dehalogenation of most of the injected dose resulted in stomach and thyroid uptake of ^{125}I. Similarly, in the WT mice at 4 h pi, only organified $^{125}I^-$ within the thyroid was consistently visible.

To assess the specificity of each peptide for binding to amyloid deposits within the organs and tissues at the cellular level, we performed microautoradiography on excised sections of liver and spleen—the major sites of amyloid deposition and proven peptide accumulation. The presence of ^{125}I-labeled peptide was evidenced as black silver grains in the emulsion (Fig. 3), and the grain density reflected the concentration of the radiolabeled peptide. In the liver, ^{125}I-labeled peptides were seen in the perivascular amyloid deposits as well as within the hepatic sinusoids corresponding to the pattern of Congo red-stained birefringent material (amyloid fibrils) in consecutive tissue sections. In the spleen, radiolabeled peptides were observed in the eosinophilic amyloid material in the perifollicular regions. Little or no uptake of any peptide was observed in association with the hepatocytes, amyloid-free hepatic sinusoids, or amyloid-free splenic follicles. Considerable differences in the grain density were found for all peptides in both tissues. The ^{125}I-p5 peptide, consistent with previous data, was present at the highest density in both hepatic and splenic amyloid deposits, although the liver appeared to exhibit a greater density per unit area of amyloid compared with the spleen (Fig. 3). The peptides ^{125}I-p1, -p4, and -p6 were also visualized as preferentially associated within

Table 1. Summary of peptide primary structures and physical data

Peptide	Amino acid sequence	Net charge	<H>*	pI	Ref.
p1	CGGYS SSRPV RRRRR PRVSR RRRRG GRRRR	+16	−0.331	12.6	49
p2	CGGYG DAKKK KDGKK AEPKN PRENK LKQPG	+6	−0.239	9.85	50
p3	CGGYP KKGSK KAVTK AQKKD GKKR	+9	−0.235	10.37	51
p4	CGGYS RPRAR ARARD QTR	+5	−0.149	11.71	52
p5	CGGYS KAQKA QAKQA KQAQK AQKAQ AKQAK Q	+8	−0.150	10.31	53
p6	CGGYP RRRRS SSRPI RRRRP RRASRR	+13	−0.251	12.52	49
p7	CGGYF AKLNC RLYRK ANKSS K	+6	0.169	10.04	54

*Hydrophobicity was calculated at http://heliquest.ipmc.cnrs.fr.
pI, isoelectric point.

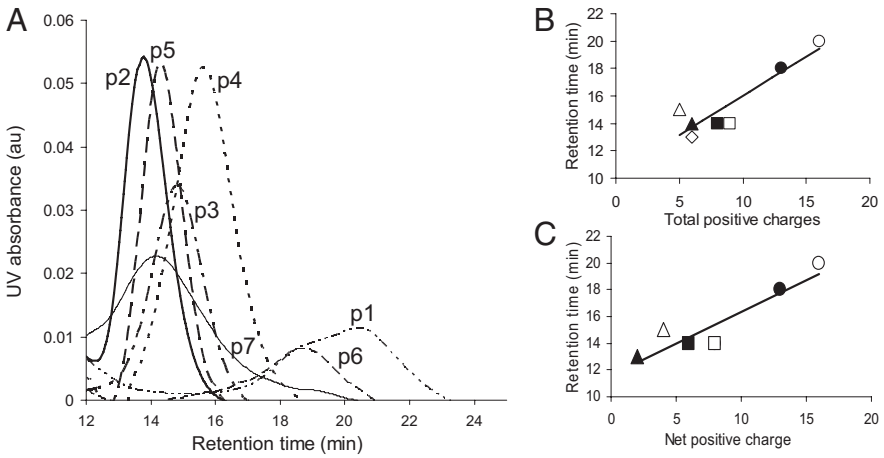

Fig. 1. Characterization of peptide binding to column-bound heparin. (*A*) Elution profiles for each peptide as the NaCl concentration increased from 0 to 2 M. Column retention of each peptide was linearly proportional to the total (*B*) and net (*C*) number of positive charges. (*B*) ○, p1; ●, p6; □, p5; ◇, p3; ■, p7; △, p4; ▲, p2. (*C*) ○, p1; ●, p6; □, p3; ■, p5; △, p4; ▲, p7.

amyloid deposits but to a lesser extent than p5. Qualitative assessment of grain density in tissue sections indicated that the amyloid-binding efficacy of each peptide decreased: p5 > p1 > p6 > p4 > p2 > p7 ~ p3. Specific accumulation of ^{125}I-labeled peptide p5 was also observed autoradiographically in the amyloid-laden intestine of ApoA2c-expressing transgenic mice, indicating that this reagent may possess panamyloid reactivity (i.e., independent of the precursor protein from which the amyloid is composed) (Fig. S2).

Based on all of the preceding assessments of amyloid reactivity, peptides p1 and p5 proved to bind specifically and at high density to amyloid in mice with AA. We, therefore, studied the kinetics of this interaction by examining peptide p1 and p5 binding in vivo at time points up to 24 h pi (Fig. 4). There was a rapid loss of ^{125}I-labeled peptide from all amyloid-free tissues examined as measured by tissue radioactivity counting (Fig. 4 *A* and *D*). In contrast, both ^{125}I-p1 and -p5 were selectively retained in the liver, spleen, and pancreas of clinically affected AA mice. Of these two peptides, retention was higher at all time points in the mice administered ^{125}I-p5 peptide compared with ^{125}I-p1 (Fig. 4 *B* and *E*). Furthermore, ^{125}I-p5 signal was preserved within the upper intestines and kidneys at 24 h pi relative to the signal seen in WT mice. Whole-body clearance of radioiodide was measured. The $T_{1/2eff}$ values for p1 and p5 in WT mice were similar and calculated to be 1.2 ± 0.01 and 1.1 ± 0.1 h, respectively. In contrast, $T_{1/2eff}$ values in AA mice were found to be 3.3 ± 0.08 and 2.3 ± 0.3 h, respectively. Notably, in AA mice administered ^{125}I-p5, there was ~50% retention of whole-body radioactivity at 24 h pi compared with <10% for all other mice examined in this study (Fig. 4 *C* and *F*). The loss of (amyloid-bound) ^{125}I-p5 from mice at time points greater than 24 h was not determined.

SPECT imaging confirmed that, at 24 h pi, ^{125}I-p5 was readily visible in the liver and spleen of mice with AA (when the thyroid activity was removed from the image); in contrast, ^{125}I-p1 was not detected in SPECT images at 8 or 24 h pi in AA mice (Fig. 4 *G–J*). These data suggested that radioiodinated peptide p5 was able to specifically image amyloid in situ up to 24 h pi (AA to WT spleen ratio at 24 h pi was 441:1). To confirm that p5 was binding to amyloid-containing areas of tissue, we examined 11 tissues using microautoradiography and correlated the distribution with Congo red-stained consecutive tissue sections (Fig. 5 shows images of eight tissues). ^{125}I-p5 peptide was observed in amyloid deposits within the spleen, liver, heart, renal papilla, renal cortex, pancreas, intestinal villi, adrenal gland, large intestine, muscle, lung, and gastric stomach, which was evidenced by the black silver grains; the location correlated precisely with the amyloid deposits seen as blue-gold birefringence in sequential Congo red-stained tissue sections (Fig. 5).

To further correlate the uptake of p5 with the amount of amyloid burden in mice, the in vivo retention of ^{125}I-p5 peptide in the spleen and liver of AA mice (n = 25) at 3 or 5 wk post-

Table 2. Percent ID per gram ^{125}I-peptide in AA mice at 1 h pi (n = 3)

	Peptide percent ID per gram (mean ± SD)						
	p1	p2	p3	p4	p5	p6	p7
Muscle	1.2 ± 0.1	1.4 ± 0.4	1.1 ± 0.1	0.9 ± 0.2	0.6 ± 0.0	0.9 ± 0.1	1.3 ± 0.2
Liver	11.6 ± 3.4	3.1 ± 1.0	6.0 ± 1.4	5.8 ± 0.7	12.5 ± 2.5	6.6 ± 1.5	4.1 ± 0.1
Pancreas	7.1 ± 2.1	3.5 ± 1.4	5.6 ± 2.3	6.3 ± 1.9	10.0 ± 4.5	4.8 ± 0.3	3.7 ± 0.5
Spleen	11.5 ± 2.2	2.4 ± 0.4	3.0 ± 1.7	5.6 ± 0.4	15.9 ± 5.2	6.3 ± 0.4	2.8 ± 0.6
L kidney	5.9 ± 0.3	12.2 ± 6.9	5.0 ± 0.2	3.6 ± 0.3	8.7 ± 2.3	3.5 ± 0.4	4.2 ± 0.6
Stomach	26.4 ± 5.8	23.9 ± 9.5	22.6 ± 3.3	20.3 ± 4.4	12.2 ± 0.9	18.1 ± 0.5	23.1 ± 2.8
Small intestine	4.6 ± 0.5	2.4 ± 0.2	2.2 ± 0.4	2.9 ± 0.7	5.3 ± 1.5	3.5 ± 1.7	2.9 ± 0.2
Large intestine	3.1 ± 0.4	2.2 ± 0.3	2.0 ± 0.1	2.6 ± 0.7	4.9 ± 1.8	2.3 ± 0.2	2.5 ± 0.5
Heart	3.1 ± 0.3	2.3 ± 0.5	2.6 ± 0.1	2.1 ± 0.5	2.7 ± 0.1	2.3 ± 0.2	3.3 ± 0.2
Lung	3.9 ± 0.1	4.3 ± 1.1	3.7 ± 0.1	3.1 ± 0.6	1.6 ± 0.2	3.1 ± 0.3	4.5 ± 1.0
Tongue	nd	nd	3.8 ± 1.6	3.8 ± 1.7	nd	nd	nd

nd, not determined; L kidney, left kidney.

Table 3. Percent ID per gram ^{125}I-peptide in WT mice at 1 h pi (n = 3)

	Peptide percent ID per gram (mean ± SD)						
	p1	p2	p3	p4	p5	p6	p7
Muscle	1.4 ± 0.2	1.3 ± 0.4	0.7 ± 0.1	0.8 ± 0.3	1.0 ± 0.3	1.0 ± 0.0	1.5 ± 0.3
Liver	6.4 ± 3.4	2.8 ± 0.1	2.4 ± 0.6	2.6 ± 0.1	3.6 ± 1.1	4.0 ± 0.7	4.6 ± 1.1
Pancreas	3.0 ± 0.5	2.4 ± 0.1	1.9 ± 0.8	1.9 ± 0.1	3.0 ± 0.7	3.0 ± 1.1	3.5 ± 2.6
Spleen	5.6 ± 3.9	2.5 ± 0.9	1.4 ± 0.1	1.6 ± 0.2	2.0 ± 0.2	3.2 ± 3.2	6.6 ± 1.7
L kidney	5.0 ± 1.0	8.9 ± 0.7	4.1 ± 0.4	3.2 ± 0.5	7.8 ± 1.8	3.8 ± 0.5	4.2 ± 0.6
Stomach	29.9 ± 6.1	29.5 ± 5.8	19.2 ± 4.7	29.5 ± 6.1	30.3 ± 3.4	19.7 ± 4.0	38.2 ± 8.4
Small intestine	4.5 ± 0.7	2.8 ± 0.6	2.7 ± 0.8	2.0 ± 0.2	5.0 ± 1.4	2.0 ± 0.2	2.6 ± 0.8
Large intestine	3.1 ± 0.1	2.1 ± 0.1	1.4 ± 0.1	1.7 ± 0.2	2.3 ± 0.3	2.1 ± 0.3	2.3 ± 0.3
Heart	3.7 ± 1.0	2.2 ± 0.3	1.8 ± 0.3	1.6 ± 0.1	2.0 ± 0.4	2.7 ± 0.4	2.8 ± 0.4
Lung	5.1 ± 0.5	3.9 ± 0.4	2.8 ± 0.3	2.9 ± 0.2	3.9 ± 0.6	4.2 ± 0.4	3.7 ± 1.7
Tongue	nd	nd	2.4 ± 0.0	4.2 ± 0.7	nd	nd	nd

nd, not determined.

amyloid enhancing factor (AEF) was determined by measuring the percent ID per gram. This finding was compared with the amyloid load based on a qualitative (0–4+) scoring of the amyloid content in 6-μm-thick tissue sections stained with Congo red and observed microscopically by polarized illumination (Fig. 6). There was a positive, significant correlation between the two metrics in both the liver (Spearman correlation coefficient = 0.95; $P = 9 \times 10^{-13}$) and spleen (0.84; $P = 1 \times 10^{-7}$).

Finally, we deemed it imperative to show that peptide p5 amyloid binding was not limited only to murine amyloids. We, therefore, began by showing immunohistochemically the presence of HSPG in human tissues containing Aβ, AL, or AA amyloid and showed a precise colocalization of the HSPG reactive mAb with sites of amyloid deposition (Fig. S3), which was confirmed by Congo red staining. We also showed the reactivity of the biotinylated p5 peptide with human ALκ, ALλ, ATTR, and AA amyloid as well as the vascular and core amyloid deposits composed of the Aβ peptide seen in patients with Alzheimer's disease (Fig. 7). In each case, the peptide bound specifically to the amyloid within the tissue sections, which was evidenced by the discrete brown staining of the amyloid (Fig. 7). No binding to amyloid-free areas of the tissue was observed as judged by Congo red staining on consecutive tissues.

Discussion

Peripheral amyloidoses are relatively rare (5,000 new cases annually in the United States) disorders caused by the insidious accumulation of protein fibrils and HSPGs in vital organs and

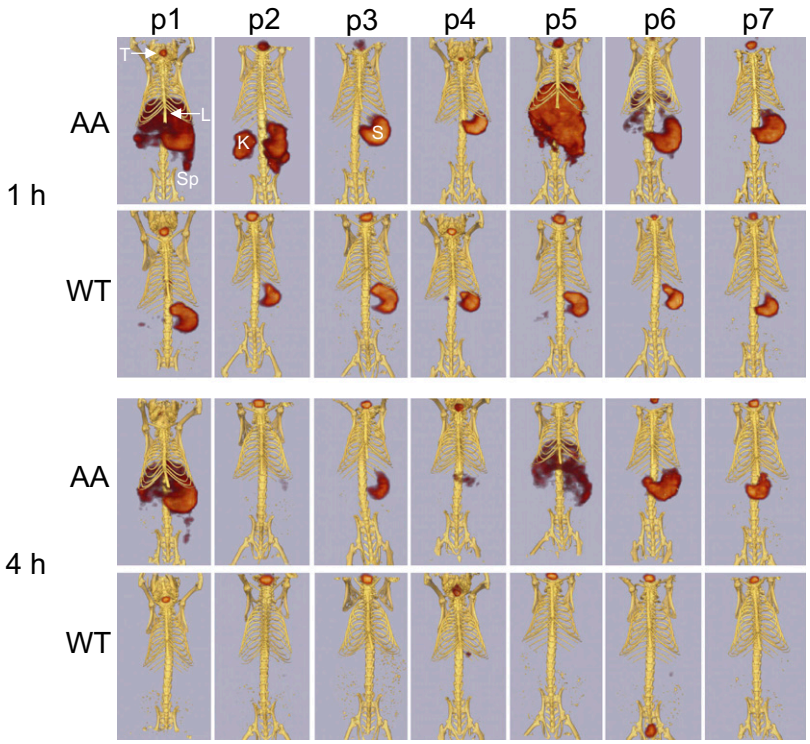

Fig. 2. SPECT/CT imaging of ^{125}I-labeled peptides in AA and WT mice at 1 and 4 h pi. SPECT and CT images were coregistered manually as described in *Materials and Methods*. For the purpose of comparison, the SPECT image volume rendering was thresholded to 60% of the maximum pixel intensity. All views are ventral, and the positions of the thyroid (T), liver (L), stomach (S), spleen (Sp), and kidney (K) are identified in *Upper*. Note that only p1 and p5 are capable of imaging amyloid-laden organs (liver and spleen) at 4 h.

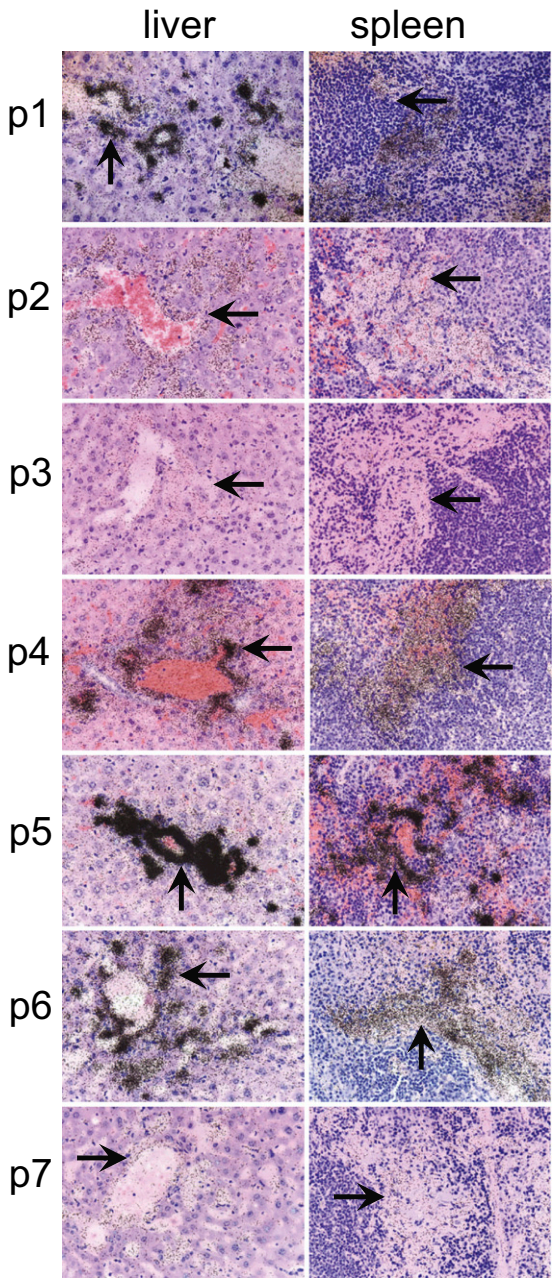

Fig. 3. Microautoradiography of ^{125}I-labeled peptides in the liver or spleen of AA mice at 1 h pi. Tissue sections from mice injected i.v. with ^{125}I-labeled peptides and euthanized at 1 h pi were exposed to photographic emulsion for 96 h before being developed. Radiolabeled peptide was visualized as punctate silver grains (arrows). (Magnification: 40×.) For display, the images were scaled to 10% of their original size.

tissues that lead to organ dysfunction and mortality (31). Currently, in the United States, there are no reliable methods to document the extent of amyloid deposition (or its resolution) in patients, and thus, there is a critical need for an objective means to assist in diagnosis and prognosis as well as to ascertain treatment efficacy or relapse.

Routine imaging techniques (CT, MRI, and ultrasound) are not particularly informative or amyloid-specific; furthermore, the deposits are rarely visualized with routine nuclear medicine agents. Although European investigators have imaged amyloid by planar gamma scintigraphy using ^{123}I-labeled P-component (9) or ^{99m}Tc-labeled aprotinin (28), these compounds are not approved in the United States by the Food and Drug Administration; furthermore, planar scintigraphy or even tomographic SPECT imaging does not provide quantitative data. Recently, we have performed a biodistribution study by using PET/CT imaging of AL patients using the ^{124}I-labeled amyloid fibril-binding mAb 11–1F4 (32). These data were collected to support the use of 11–1F4 as an immunotherapeutic reagent for patients with AL. Although we were able to show specific colocalization of the antibody with AL amyloid in ~60% of the patients imaged to date (n = 38), it failed to image amyloid in all patients. Notably, amyloid in heart and kidneys (two organs most prone to fatal failure because of amyloid burden) was rarely, if ever, imaged. Therefore, the 11–1F4 mAb will likely not be an effective first-line diagnostic and disease-monitoring reagent for all patients. Thus, with the continuing need to determine the presence and biodistribution of amyloid in the major target organs of patients and those subjects entered in therapeutic clinical trials, we have evaluated the use of amyloid-associated HSPG as a target for imaging because of its ubiquitous presence in high concentrations of all amyloid deposits, irrespective of the nature of the fibril protein. We have used small peptide probes that bind amyloid-associated HSPG. These peptides can be chemically synthesized, have a better likelihood of extravasation (compared with larger proteins such as SAP or 11–1F4), and may provide better imaging of extravascular amyloid deposits.

The HSPG in amyloid has been shown to be biochemically distinct from the HSPG found in healthy tissues, which was evidenced by the finding that human AA amyloid-derived HS exhibited a shift in the ratio of disaccharides relative to HS from healthy tissue (17). It has also been shown that HS derived from amyloidotic spleens of CBA/J mice similarly contained a disaccharide profile that was clearly distinct from the profile obtained from amyloid-free tissue by using capillary chromatography and time of flight MS (20). In addition, we have recently shown that the HSPG in murine AA amyloid can be imaged and detected autoradiographically using radioiodinated scFvs that are reactive with specific heparan sulfate moieties (22). One scFv in particular, NS4F5, which was isolated from a phage library using human lung HS extract as the target, was found to colocalize selectively with amyloid deposits in the liver and spleen in our AA mouse model relative to healthy (amyloid-free) tissues. The precise target recognized by this reagent has been elucidated and shown by in vitro characterization to consist of HS with *N*-sulfation, C5-epimerization, and high degrees of 2-*O*- and 6-*O*-sulfation (33). These data suggest that, in addition to the high concentration of HS in amyloid deposits, it is hypersulfated relative to the ubiquitous normal tissue HS, making it structurally distinct. This combination of properties renders HSPG an important biomarker for targeting amyloid, with potential for imaging, prognostication, and monitoring response to therapy.

Increased sulfation of amyloid-associated HS renders it structurally and electrochemically similar to heparin, which unlike ubiquitous HSPG, has a limited distribution in mammals and is confined to cytoplasmic granules of mast cells. Because of the critical role played by heparin in the coagulation cascade and the importance of heparin-like binding motifs expressed by signal-transducing cellular glycosaminoglycans, there has been considerable interest in identifying and characterizing heparin-binding peptides (34). In addition, several recent in vitro studies have shown that highly sulfated heparin catalyzes the fibrillogenesis of amyloid precursor proteins, including Ig light chains, β-2-microglobulin, Aβ, and sAA, relative to less-sulfated glycosaminoglycans (35–37). Based on our hypothesis that HS in amyloid is heparin-like, we synthesized a panel of heparin-binding peptides and assessed their ability to bind amyloid in vivo. The ultimate goal was to identify reagents that, when ap-

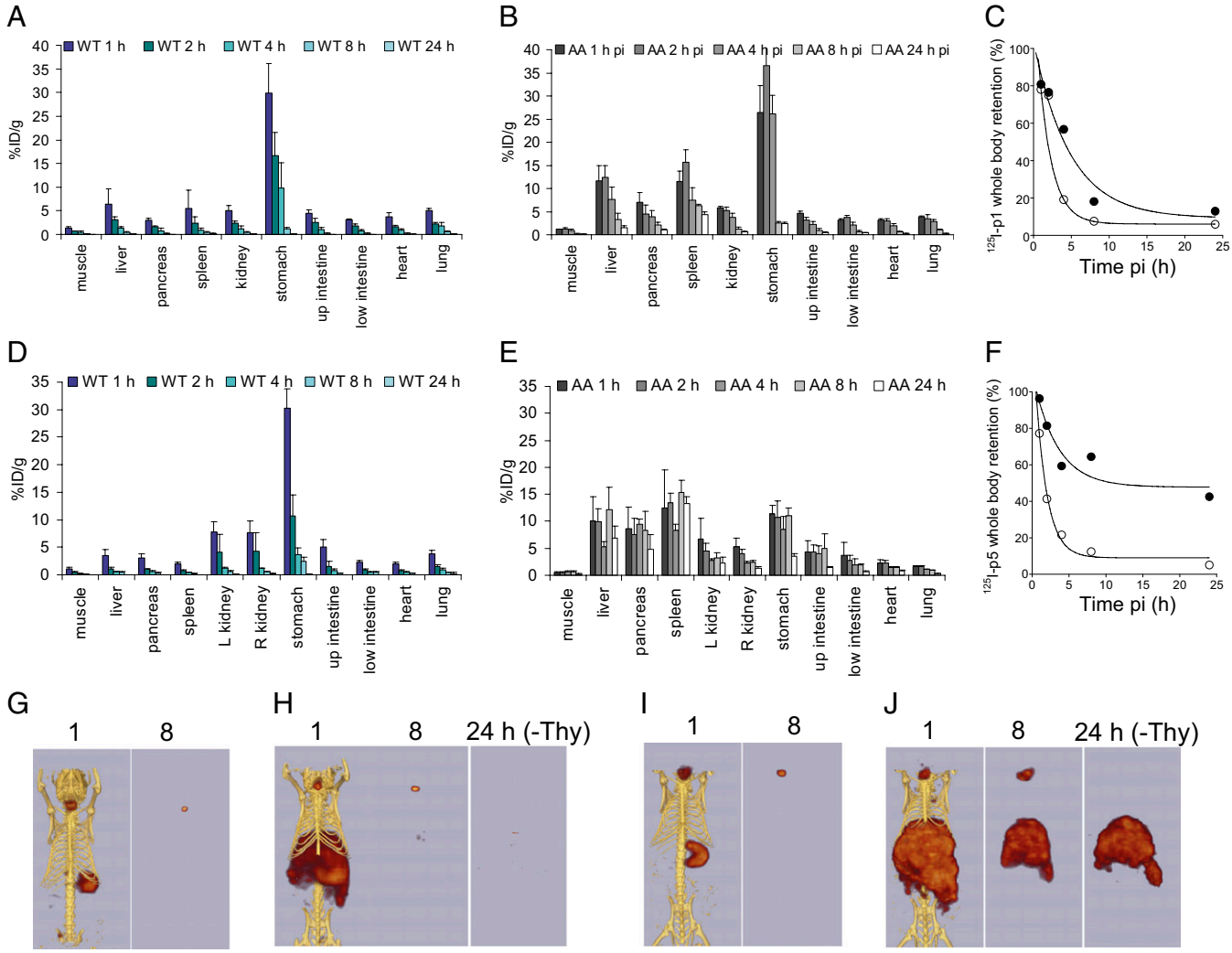

Fig. 4. Comparison of ^{125}I-labeled peptides p1 and p5 in AA and WT mice at time points up to 24 h pi. Tissue biodistribution of ^{125}I-p1 (*A* and *B*) and ^{125}I-p5 (*D* and *E*) in WT and AA mice at 1, 2, 4, 8, and 24 h pi expressed as the mean ± SD (n = 3). Representative whole-body clearance of ^{125}I-p1 (*C*) and ^{125}I-p5 (*F*) is shown for AA (●) or WT (○) mice, where curves are single exponential decay fits to the data. Note retention of the peptide p5 in mice with AA. SPECT/CT imaging of ^{125}I-p1 and -p5 in control WT mice (*G* and *I*, respectively) and AA mice (*H* and *J*, respectively). Images of peptides in WT mice at 24 h were negative. All images are ventral views, with the volume-rendering threshold scaled to 50% of the maximum intensity. The thyroid activity was cropped (−Thy) from the 24-h images before applying the threshold.

propriately labeled, may prove to be efficacious imaging agents for diagnosis and disease monitoring.

We focused our attention on the evaluation of heparin-binding peptides rather than scFv or antibodies, because peptides can be chemically synthesized, are rapidly cleared from the circulation when not bound to target, are relatively small, can penetrate blood vessel walls, and are generally nonimmunogenic—all desirable properties of tracers for molecular imaging in man (38–41). Of the seven peptides that we have evaluated in this study, one in particular, p5, was shown to bind specifically and selectively to murine AA amyloid in vivo, which was evidenced in tissue biodistribution studies in which the target organ to muscle ratios were calculated to be between 15:1 and 30:1 in amyloid-containing tissues (corresponding to ∼5–16% ID/g). To monitor changes in amyloid load (either progression or regression in response to therapy), it is important to show that retention of the amyloid imaging radiotracer varied with other metrics of amyloid load. We have shown that binding of ^{125}I-p5 in the murine model of AA correlated linearly and significantly with amyloid burden based on Congo red staining. This finding suggests that amyloid imaging with p5 could provide a noninvasive method for quantifying amyloid load in vivo and a means to monitor changes in burden similar to SAP imaging (42).

The exemplary reactivity of p5 with amyloid in vivo, compared with the other peptides tested, cannot be explained simply in terms of the net charge density, because peptides p1, p3, and p6 all contain a higher charge density than p5, and consequently, they were found to bind column-associated heparin with greater avidity. Peptide p5 may preferentially bind amyloid HSPG because of its propensity to adopt an aliphatic α-helix that results in a structured, linear spacing of basic amino acid residues along one face (34). This organization may provide optimal charge spacing and subsequently, an enhanced valency of interaction relative to peptides with clustered basic amino acid residues, such as those residues found in p1 and p6.

We chose to use radioiodinated forms of each peptide, because we have shown previously and now confirmed in this study that peptides not specifically bound to extracellular amyloid are rapidly catabolized (principally by the kidneys but to a lesser extent, by the hepatobiliary system). During catabolism,

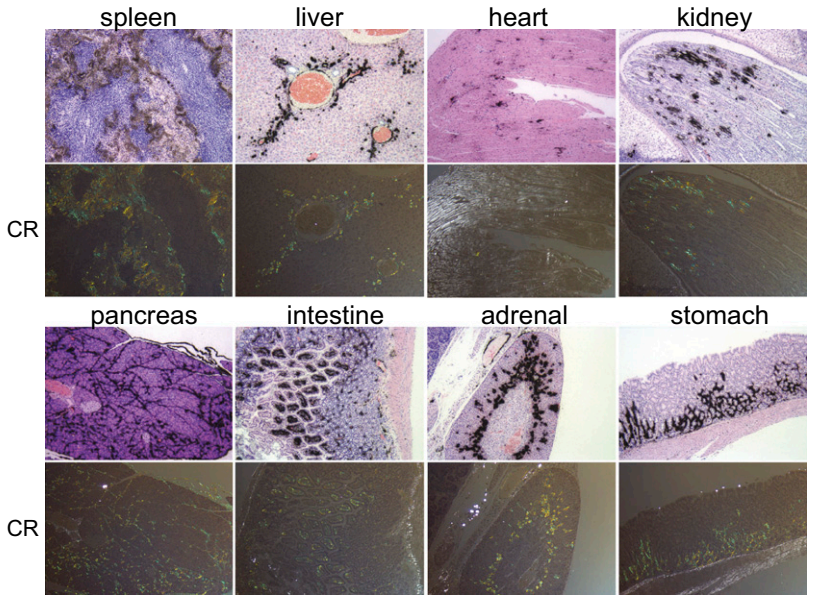

Fig. 5. Microautoradiography and Congo red staining of amyloid-laden tissues. Mice with advanced AA were injected i.v. with ^{125}I-p5 peptide and euthanized at 1 h pi. Tissues were fixed, and slides were prepared for Congo red (CR) staining or microautoradiography. For microautoradiology, tissue sections were exposed to photographic emulsion for 96 h before being developed and counterstained with H&E. Congo red staining of amyloid appears as green/yellow birefringent material in polarized light microscopy. (Magnification: 80×.) For display, the images were scaled to 10% of original size.

the peptides are dehalogenated, and the liberated $^{125}I^{-}$ reenters the circulation and is rapidly sequestered by the stomach and thyroid, leaving an essentially signal-free kidney and liver at later time points (>4 h) in mice with no amyloid in these organs. This process is advantageous and contributes significantly to generating an increased signal to noise ratio in these organs, and we posit that, at >24 h pi, renal amyloidosis may be visualized in man using peptide p5. However, ^{125}I cannot be used for imaging in man (or animals larger than a mouse) because of the low-energy gamma photons from this isotope (~30 keV) that are readily attenuated and scattered by tissues before they can be detected. Therefore, it would be necessary to develop variants of p5 peptide for clinical SPECT or PET imaging using the ^{123}I or ^{124}I isotopes, respectively. To this end, we have prepared and tested ^{124}I-p5 and shown, in preliminary results, that it provides effective PET imaging of AA amyloid.

SPECT imaging of mice with AA revealed the uptake of ^{125}I-p5 peptide in abdominal organs, including the liver, spleen, kidneys, and arguably, pancreas; however, microautoradiography confirmed that ^{125}I-p5 was present in amyloid deposits in all organs and tissues that contained amyloid (including heart, stomach, and intestines). The inability of our SPECT imaging system to detect the peptide tracer in these organs is likely because of the low sensitivity of the single pinhole collimation used to acquire the images and the low energy of the ^{125}I, leading to a low fraction of nonscattered photons. Both of these limitations can be overcome by using higher-energy radioisotopes such as ^{123}I or ^{124}I and acquiring either SPECT data with multipinhole collimation or PET images, both of which will afford higher count statistics relative to the images that we show herein.

All extracellular amyloid deposits contain significant concentrations of HSPG; however, unlike the amyloid fibril precursor proteins that often share significant primary structural homology (5), the amyloid-associated HSPG may be structurally diverse with organ or species-related specificities. To generalize our findings, we deemed it imperative to show that peptide p5 was able to bind amyloid deposits from other species and those deposits containing various fibril types. Human AL, AA, ATTR, and Aβ-containing amyloids as well as canine AA, feline islet amyloid polypeptide (AIAPP), and murine apolipoprotein A2c (ApoA2c) were histochemically stained by using biotinylated peptide p5. We hypothesize, based on the reactivity of the p5 peptide with tissue amyloid, that heparin-like HSPG is potentially a universal biomarker for amyloid, which significantly expands the potential use of peptide p5 and similar reagents as tools for detecting and targeting amyloid in vivo.

Thus, we have identified a heparin-binding peptide that, because of its structural properties, binds amyloid-associated HSPG specifically and when radioiodinated, can be used to visualize the presence of this pathology by using small animal SPECT imaging up to 24 h pi. The ability to bind many extracellular amyloid deposits, rapid loss of signal from unbound ^{125}I-p5, and lack of binding to healthy tissues support the evaluation

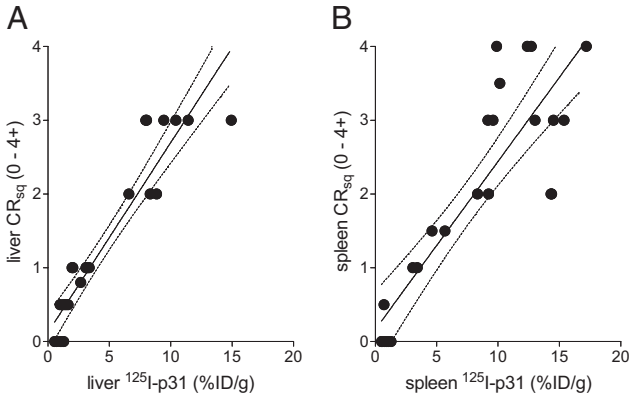

Fig. 6. Comparison of ^{125}I-p5 tissue retention with amyloid load as evidenced in Congo red-stained tissue sections. Tissue biodistribution of ^{125}I-p5 in the liver (*A*) and spleen (*B*) of AA mice at 2 h pi correlated linearly with the qualitative measure of amyloid burden (0–4+ scale) assessed in Congo red-stained tissue sections. The correlation was significant based on Spearman correlation coefficients and *P* values for the liver (0.95 and 9×10^{-13}) and spleen (0.84 and 1×10^{-7}).

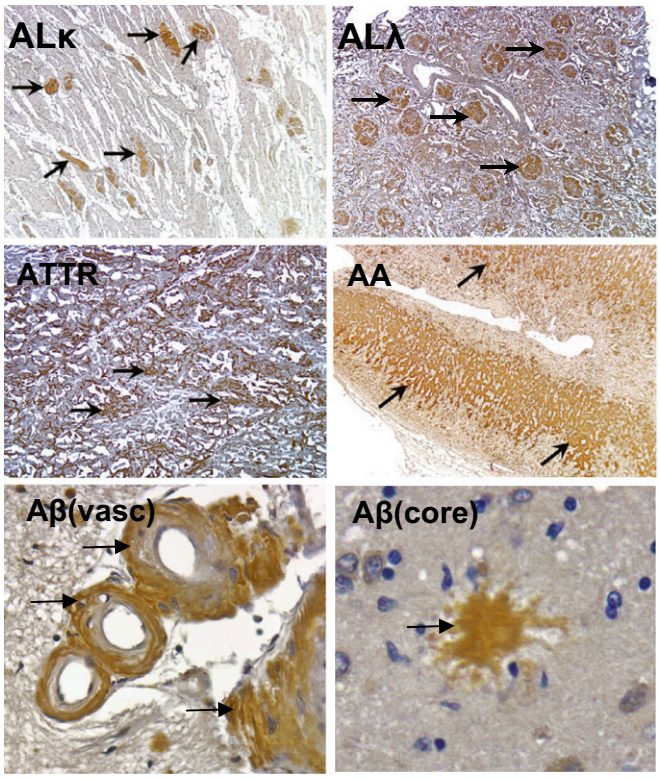

Fig. 7. Peptide histochemistry of human amyloid-containing tissues from patients with ALλ, ALκ, ATTR, AA, or Aβ. Biotinylated p5 peptide was applied to tissue sections detected by streptavidin-conjugated HRP and visualized using diaminobenzidene, rendering the specific binding of the biotinylated peptide as brown coloration (arrows). Slides were counterstained with H&E. Note staining of amyloid in perivascular (vasc) and core areas of Aβ amyloid in the human brain. (Magnification: AA, AL, and ATTR images, 40×; Aβ images, 320×.) For display, the images were scaled to 10% of original size.

of this peptide as a potential amyloid imaging agent for the noninvasive, rapid detection and monitoring of disease in patients with amyloidosis.

Materials and Methods

Peptide Synthesis and Purification. Peptides were purchased from Keck Laboratories as semipure preparations. Routine purification was performed by HPLC (1100 series; Agilent) by elution from a reverse-phase C3 matrix in a linear gradient of 0–50% acetonitrile in water with 0.05% trifluoroacetic acid. Peptide peaks were eluted from the column using a flow rate of 1 mL/min; 1-mL fractions were collected, peak fractions were pooled, and the mass was determined by MS using a single quadropole MS (Applied Biosystems).

Heparin Binding Assay. A 20-mL bed volume Heparin FF16/10 column (28-9365-49; GE Healthcare) was used with a Biorad Biologic duoflow fast protein liquid chromatography (FPLC) system. Buffer A was 20 mM Tris·HCl and 150 mM NaCl, pH 8.0, and the high-salt elution buffer B was 20 mM Tris·HCl and 2 M NaCl, pH 8.0. Peptides were monitored by UV absorbance at 280 nm, and the salt concentration was recorded by an inline conductivity meter. An aliquot of 0.5 mg peptide (1 mg/mL) suspended in buffer A with 20 μL Tris (2-carboxyethyl) phosphine reducing agent (0.5 M; Pierce) was injected over 30 s onto the heparin column. The peptides were eluted using a high-salt linear gradient from 0.15 to 2 M NaCl over 10 min with a flow rate of 2 mL/min, and 1-mL fractions of eluent were collected for ~30 min. This collection was followed by a 15-min isocratic flow of 2 M NaCl and then, a 30-min 100% buffer A isocratic flow to return the column to the starting conditions. The retention time was calculated by measuring the time at the apex of the elution peak.

Animals. AA amyloidosis was induced in H2-L^d-huIL-6 Tg BALB/c (C) transgenic mice that constitutively express the human IL-6 transgene (43, 44) by i.v. administration of 100 μg isolated AA amyloid fibrils (AEF) in 100 μL sterile PBS. The mice developed AA amyloidosis by ~3 wk post-induction. All animals used in these experiments were either 3 or 6 wk post-induction. All animal procedures were performed under the auspices of protocols approved by the University of Tennessee Animal Care and Use Committee. The University of Tennessee is an American Association for the Accreditation of Laboratory Animal Care International-accredited institution.

Peptide Radiolabeling. Peptides were radioiodinated with ^{125}I (Perkin-Elmer) using 20 μg chloramine T to protect the peptide from the effects of excessive and damaging oxidation. The radiolabeled product was diluted into 0.1% sterile gelatin in PBS and purified by gel filtration on a 5-mL PD10 column equilibrated in gelatin/PBS. Peak fractions of radioactivity were pooled, and the product's radiochemical purity was established by SDS/PAGE analyzed by a phosphor imager (Cyclone Storage Phosphor System; Perkin-Elmer).

SPECT/CT Imaging. Mice were injected with 5–10 μg ^{125}I-labeled peptide (100–200 μCi) diluted in 5 mg/mL gelatin/PBS (200 μL final volume) in the lateral tail vein and then, housed in a satellite facility with food and water provided ad libitum for 1–24 h in a 12-h light and dark cycle. At the predetermined times pi, the mice were euthanized by an isoflurane inhalation overdose using the drop chamber before imaging and necropsy.

SPECT and CT images were acquired using a microCAT II + SPECT imaging platform (Siemens) (45). Mice were positioned prone on a cardboard platform, and the board was placed on the scanner bed (46). CT data were acquired using an X-ray voltage biased to 80 kVp with a 500-μA anode current and the data binned at 4 × 4. A 475-ms exposure was used, and 360 1° projections were collected. The data were reconstructed using an implementation of the Feldkamp filtered back-projection algorithm (47) onto a 512 × 512 × 768 matrix with isotropic 0.077-mm voxels.

SPECT images were collected using a 2-mm diameter pinhole collimator positioned 50 mm from the center of the field of view. Each dataset comprised 40 projections, with a 60-s exposure at each azimuth. A total of 0.5 × 10^6 events was acquired by both detectors. Data from both SPECT heads were reconstructed posthoc onto an 88 × 88 × 116 matrix with isotropic 0.86-mm voxels using a 3D ordered subset expectation maximization algorithm with eight iterations and four subsets.

SPECT/CT Image Analysis. CT and SPECT datasets were imported into a 3D visualization software package (Amira Version 4.1.0; Mercury Computer Systems) and coregistered. All images were rendered using the same visualization parameters in Amira.

Biodistribution. Samples of muscle, liver, spleen, pancreas, kidney, heart, tongue, stomach, small and large intestines, and lung tissue were harvested postmortem from every mouse (46). Each sample was placed into a tared plastic vial and weighed, and the ^{125}I radioactivity was measured using an automated Wizard 3 gamma counter (1480 Wallac Gamma Counter; Perkin-Elmer). The biodistribution data were expressed as percent injected dose per gram tissue. In addition, samples of each tissue were fixed in 10% buffered formalin for 24 h and embedded in paraffin for histology and autoradiography.

Microautoradiography and Congo Red Staining. For autoradiography, 4- to 6-μm-thick sections were cut from formalin-fixed, paraffin-embedded blocks onto Plus microscope slides (Fisher Scientific), dipped in NTB-2 emulsion (Eastman Kodak), stored in the dark, and developed after a 96-h exposure. Each section was counterstained with hematoxylin. Tissue amyloid deposits were microscopically confirmed in consecutive tissue sections viewed under cross-polarized illumination after staining with alkaline Congo red. Blinded qualitative assessment of amyloid load in Congo red-stained sections of liver and spleen was performed by ranking each tissue on a 0–4+ scale, and it was based not only on the area of tissue occupied by the amyloid but also on the distribution of the deposits within the tissue. All tissue sections were examined using a Leica DM500 light microscope fitted with cross-polarizing filters. Digital microscopic images were acquired using a cooled CCD camera (SPOT; Diagnostic Instruments).

Measurement of Whole-Body Radioactivity Clearance. Single-animal in vivo whole-body clearance measurements were performed in mice injected with ~10 μg (200 μCi) ^{125}I-p1 or -p5. The unanesthetized mice were placed at various time intervals in a plastic chamber and lowered into a commercial PET dose calibrator (CRC–15 PET; Capintec) that had been calibrated using

known reference standards. Multiple readings were acquired over a 24-h period, and the data were analyzed using monoexponential kinetics. Because of the long physical half-life of ^{125}I, the effective half-life ($T_{1/2eff}$) for both peptides was essentially equivalent to the measured biologic half-life ($T_{1/2bio}$). This assumption was validated by calculating $T_{1/2eff}$ as described previously (48).

Tissue Staining with Biotinyl-p5 Peptide (Peptide Histochemistry). Peptide p5 was prepared for tissue staining by biotinylation according to the manufacturer's instructions using a maleimide-biotin conjugation kit (Pierce); 6-μm-thick formalin-fixed, paraffin-embedded tissue sections were placed on slides and incubated in citrate antigen retrieval solution (Citrus Plus; Bio-Genex) at 90 °C for 30 min, and then, the biotinylated peptide p5 was added at a concentration of 5 μg/mL in PBS and incubated overnight at 4 °C. The slides were developed using the Vectastain Elite ABC development kit (Vector Labs) and visualized using diaminobenzidene (Vector Labs).

ACKNOWLEDGMENTS. We thank Craig Wooliver for performing Congo red staining and Charles Murphy for assistance with the MS analyses. Ying Huang assisted S.J.K. with the biodistribution measurements. The project described was supported by National Institute of Diabetes and Digestive and Kidney Diseases Award R01DK079984.

1. Merlini G, Bellotti V (2003) Molecular mechanisms of amyloidosis. *N Engl J Med* 349: 583–596.
2. Pepys MB (2006) Amyloidosis. *Annu Rev Med* 57:223–241.
3. Lachmann HJ, Hawkins PN (2006) Systemic amyloidosis. *Curr Opin Pharmacol* 6: 214–220.
4. Goldsbury C, et al. (2011) Amyloid structure and assembly: Insights from scanning transmission electron microscopy. *J Struct Biol* 173:1–13.
5. Nelson R, Eisenberg D (2006) Recent atomic models of amyloid fibril structure. *Curr Opin Struct Biol* 16:260–265.
6. Kahn SE, Andrikopoulos S, Verchere CB (1999) Islet amyloid: A long-recognized but underappreciated pathological feature of type 2 diabetes. *Diabetes* 48:241–253.
7. Kisilevsky R, Ancsin JB, Szarek WA, Petanceska S (2007) Heparan sulfate as a therapeutic target in amyloidogenesis: Prospects and possible complications. *Amyloid* 14:21–32.
8. Ohashi K (2001) Pathogenesis of beta2-microglobulin amyloidosis. *Pathol Int* 51:1–10.
9. Hawkins PN, Pepys MB (1995) Imaging amyloidosis with radiolabelled SAP. *Eur J Nucl Med* 22:595–599.
10. Linke RP (2000) Highly sensitive diagnosis of amyloid and various amyloid syndromes using Congo red fluorescence. *Virchows Arch* 436:439–448.
11. Wu C, Wang Z, Lei H, Zhang W, Duan Y (2007) Dual binding modes of Congo red to amyloid protofibril surface observed in molecular dynamics simulations. *J Am Chem Soc* 129:1225–1232.
12. Ancsin JB (2003) Amyloidogenesis: Historical and modern observations point to heparan sulfate proteoglycans as a major culprit. *Amyloid* 10:67–79.
13. Li JP, et al. (2005) In vivo fragmentation of heparan sulfate by heparanase overexpression renders mice resistant to amyloid protein A amyloidosis. *Proc Natl Acad Sci USA* 102:6473–6477.
14. Snow AD, Bramson R, Mar H, Wight TN, Kisilevsky R (1991) A temporal and ultrastructural relationship between heparan sulfate proteoglycans and AA amyloid in experimental amyloidosis. *J Histochem Cytochem* 39:1321–1330.
15. Inoue S, Hultin PG, Szarek WA, Kisilevsky R (1996) Effect of poly(vinylsulfonate) on murine AA amyloid: A high-resolution ultrastructural study. *Lab Invest* 74:1081–1090.
16. Dember LM, et al. (2007) Eprodisate for the treatment of renal disease in AA amyloidosis. *N Engl J Med* 356:2349–2360.
17. Lindahl B, Lindahl U (1997) Amyloid-specific heparan sulfate from human liver and spleen. *J Biol Chem* 272:26091–26094.
18. Snow AD, Kisilevsky R, Stephens C, Anastassiades T (1987) Characterization of tissue and plasma glycosaminoglycans during experimental AA amyloidosis and acute inflammation. Qualitative and quantitative analysis. *Lab Invest* 56:665–675.
19. Stenstad T, Magnus JH, Husby G (1994) Characterization of proteoglycans associated with mouse splenic AA amyloidosis. *Biochem J* 303:663–670.
20. Sugumaran G, et al. (2004) Characterization of splenic glycosaminoglycans accumulated in vivo in experimentally induced amyloid-susceptible and amyloid-resistant mice. *Scand J Immunol* 60:574–583.
21. Bruinsma IB, et al. (2010) Sulfation of heparan sulfate associated with amyloid-beta plaques in patients with Alzheimer's disease. *Acta Neuropathol* 119:211–220.
22. Smits NC, et al. (2010) The heparan sulfate motif (GlcNS6S-IdoA2S)3, common in heparin, has a strict topography and is involved in cell behavior and disease. *J Biol Chem* 285:41143–41151.
23. Hazenberg BP, et al. (2006) Diagnostic performance of 123I-labeled serum amyloid P component scintigraphy in patients with amyloidosis. *Am J Med* 119:355.e15–355.e24.
24. Rydh A, et al. (1998) Serum amyloid P component scintigraphy in familial amyloid polyneuropathy: Regression of visceral amyloid following liver transplantation. *Eur J Nucl Med* 25:709–713.
25. Tan SY, et al. (1996) Long term effect of renal transplantation on dialysis-related amyloid deposits and symptomatology. *Kidney Int* 50:282–289.
26. Glaudemans AW, et al. (2009) Nuclear imaging in cardiac amyloidosis. *Eur J Nucl Med Mol Imaging* 36:702–714.
27. Han S, et al. (2007) Preliminary experience of 99mTc-Aprotinin scintigraphy in amyloidosis. *Eur J Haematol* 79:494–500.
28. Schaadt BK, et al. (2003) 99mTc-aprotinin scintigraphy in amyloidosis. *J Nucl Med* 44: 177–183.
29. Puille M, et al. (2002) 99mTc-DPD scintigraphy in transthyretin-related familial amyloidotic polyneuropathy. *Eur J Nucl Med Mol Imaging* 29:376–379.
30. Rapezzi C, Guidalotti P, Salvi F, Riva L, Perugini E (2008) Usefulness of 99mTc-DPD scintigraphy in cardiac amyloidosis. *J Am Coll Cardiol* 51:1509–1510.
31. Comenzo RL (2006) Amyloidosis. *Curr Treat Options Oncol* 7:225–236.
32. Wall JS, et al. (2010) Radioimmunodetection of amyloid deposits in patients with AL amyloidosis. *Blood* 116:2241–2244.
33. Wijnhoven TJ, et al. (2008) Characterization of anticoagulant heparinoids by immunoprofiling. *Glycoconj J* 25:177–185.
34. Rullo A, Nitz M (2010) Importance of the spatial display of charged residues in heparin-peptide interactions. *Biopolymers* 93:290–298.
35. Ren R, et al. (2010) Role of glycosaminoglycan sulfation in the formation of immunoglobulin light chain amyloid oligomers and fibrils. *J Biol Chem* 285: 37672–37682.
36. Ariga T, Miyatake T, Yu RK (2010) Role of proteoglycans and glycosaminoglycans in the pathogenesis of Alzheimer's disease and related disorders: Amyloidogenesis and therapeutic strategies—a review. *J Neurosci Res* 88:2303–2315.
37. Corlin DB, Johnsen CK, Nissen MH, Heegaard NH (2010) Glycosaminoglycans enhance the fibrillation propensity of the β2-microglobulin cleavage variant—ΔK58-β2m. *Biochem Biophys Res Commun* 402:247–251.
38. Lee S, Xie J, Chen X (2010) Peptide-based probes for targeted molecular imaging. *Biochemistry* 49:1364–1376.
39. Reubi JC, Maecke HR (2008) Peptide-based probes for cancer imaging. *J Nucl Med* 49: 1735–1738.
40. Riccabona G, Decristoforo C (2003) Peptide targeted imaging of cancer. *Cancer Biother Radiopharm* 18:675–687.
41. Schottelius M, Wester HJ (2009) Molecular imaging targeting peptide receptors. *Methods* 48:161–177.
42. Hawkins PN (1994) Diagnosis and monitoring of amyloidosis. *Baillieres Clin Rheumatol* 8:635–659.
43. Solomon A, et al. (1999) Transgenic mouse model of AA amyloidosis. *Am J Pathol* 154: 1267–1272.
44. Wall JS, et al. (2008) Quantitative tomography of early-onset spontaneous AA amyloidosis in interleukin 6 transgenic mice. *Comp Med* 58:542–550.
45. Gregor J, et al. (2006) A micro-SPECT/CT system for imaging of AA-amyloidosis in mice. *Small-Animal SPECT Imaging*, eds Kupinski M, Barrett H (Plenum, New York), pp 209–213.
46. Wall JS, et al. (2006) Micro-imaging of amyloid in mice. *Methods Enzymol* 412: 161–182.
47. Feldkamp LA, Davis LC, Kress JW (1984) Practical cone-beam algorithm. *J Opt Soc Am* 1:612–619.
48. Wall JS, et al. (2006) Radioimaging of light chain amyloid with a fibril-reactive monoclonal antibody. *J Nucl Med* 47:2016–2024.
49. Liang JF, Yang VC, Vaynshteyn Y (2005) The minimal functional sequence of protamine. *Biochem Biophys Res Comm* 336(2):653–659.
50. Ancsin JB, Kisilevsky R (2004) A binding site for highly sulfated heparan sulfate is identified in the N terminus of the circumsporozoite protein: significance for malarial sporozoite attachment to hepatocytes. *J Biol Chem* 279(21):21824–21832.
51. Watson K, Gooderham NJ, Davies DS, Edwards RJ (1999) Nucleosomes bind to cell surface proteoglycans. *J Biol Chem* 274(31):21707–21713.
52. Wang J, Rabenstein DL (2009) Interaction of heparin and heparin-derived oligosaccharides with synthetic peptide analogues of the heparin-binding domain of heparin/heparan sulfate-interacting protein. *Biochim Biophys Acta* 1790(12):1689–1697.
53. Jayaraman G, et al. (2000) Binding of a de novo designed peptide to specific glycosaminoglycans. *FEBS Lett* 482(1–2):154–158.
54. Onoue S, Nemoto Y, Harada S, Yajima T, Kashimoto K (2003) Human antithrombin III-derived heparin-binding peptide, a novel heparin antagonist. *Life Sci* 73(22): 2793–2806.